Modeling of Bubble Transportation, Expansion, as Well as Adhesion of Inclusions in a Ladle With Different Tuyeres

XIANGLONG LI, DEYONG WANG, JUN TIAN, HUIHUA WANG, TIANPENG QU, DONG HOU, SHAOYAN HU, ZHIXIAO ZHANG, XINGZHI ZHOU, and GUANGJUN WU

A new model is developed to describe the coalescence and breakup between bubbles and inclusions. In this model, the density of bubble attached inclusions is calculated through mass conservation equation. The momentum exchange after breakup or coalescence is derived through momentum conservation equation, which are tracked by discrete particle method (DPM). Three continuous phases (air-slag-steel) are considered in a ladle, and the unsteady turbulent flow is computed through k-ε method. What's more, bubble expansion due to decreasing of hydraulic pressure is also taken into account. Results show that due to the bubble expansion, bubble density is mostly decreased to 0.3 to 0.8 kg/m^3. However, after attaching some inclusions, the bubble density significantly rises to 20 to 60 kg/m^3. The optimal bubble diameters attaching inclusions are ranged between 1.5 and 10 mm. For traditional slot–slot matched tuyeres (S–S mode), the inclusion removement ratio is 29.48 pct; By comparison, after employing the slot–porous matched tuyeres (S–P mode), the inclusion removements ratio rises to 36.34 pct. The mixing time is also shortened after adopting the S–P mode. The reason for this phenomenon is because the slot tuyere produces a strong asymmetry stream that drives more liquid to flow at the bottom of the ladle. And at the same time, the porous tuyere produces more fine bubbles to entrap more inclusions to the top. Taking advantages of porous and slot tuyeres, the mixing behavior and inclusion removements improves a lot. The result is beneficial for improving ladle refining.

I. INTRODUCTION

LADLE is a steel container in which argon is injected from a bottom tuyere made up of refractory materials. In this container, argon is injected from a refractory tuyere that planted at the bottom of the ladle and purify the unnecessary hazardous elements through interactions with liquid steel. Just as shown in Figure 1, the continuous gas phase may be divided into discrete bubbles after injected from a tuyere. Bubbles may aggregate into a bigger one, break into smaller ones and expand due to decreasing of hydraulic pressure. No matter what happens, they'll finally escaped from the top of the slag, forming a plume zone above the tuyeres. A high flow rate of argon is often used to promote desulfurization and alloy mixing, however, if the flow rate exceeds a critical value, the liquid steel may splash out of the top slag, and absorb some harmful elements into the steel such as oxygen and nitrogen. By contrast, soft blowing can generate more small bubbles and stick inclusions to the surface, which is beneficial for inclusion removal, but the alloy mixing is delayed because the flow is weak. What's more, even though the inclusion modification has achieved great success in the past decades, the movements of inclusions are still not easy to control, especially with high argon flow rate. As a result, to get a non-defects clean steel without sacrificing productivity is still a hot topic for today's company.

XIANGLONG LI is with the Soochow University, Suzhou 215137, P.R. China. DEYONG WANG, JUN TIAN, HUIHUA WANG, TIANPENG QU, DONG HOU, SHAOYAN HU, ZHIXIAO ZHANG, and XINGZHI ZHOU are with the School of Iron and Steel, Soochow University, Suzhou 215137, P.R. China. Contact e-mails: dywang@suda.edu.cn; jtian@suda.edu.cn GUANGJUN WU is with the Laiwu Technique Center, Shandong Iron & Steel Group Company Limited, Jinan 271104, P.R. China.
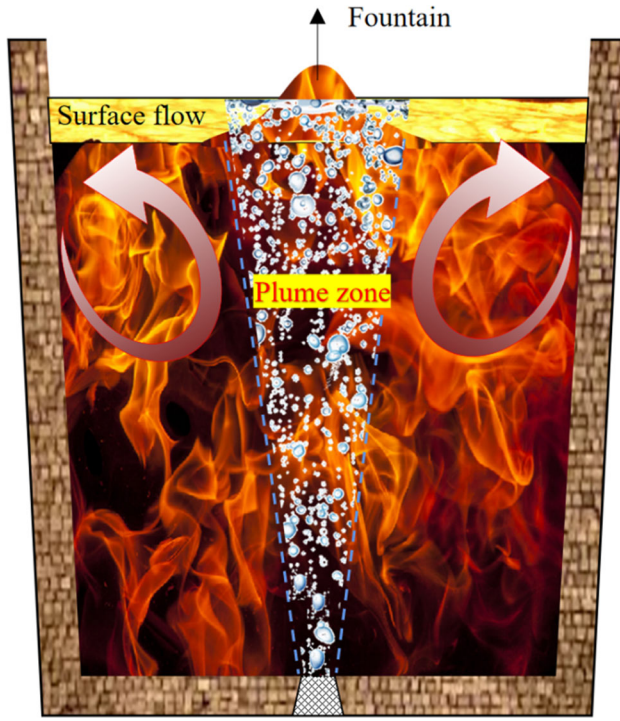
Fig. 1—Schematic diagram of bubble injection in ladle refining.

As a bubble-driven tube, no matter desulfurization, inclusion removements and chemical reactions, are all depended on the good mixing and homogenization of molten steel.[1–3] Thus the bubble generators (or tuyeres) are quite essential for the refining process. In modern refining process, two categories of tuyeres are commonly used as bubble generators: slot tuyere and porous tuyere.[4] During this process, the buoyancy force acted on bubble would drive the surrounding steel to move, and transport inclusions along streamlines. Generally speaking, two mechanisms[5] of removing inclusions are identified: one is the bubble wake, the other one is surface adhesion. Because slot tuyere has the characteristics of high breathable strength and good stirring performance, many enterprises use this kind of tuyere for secondary refining. However, the inclusion residual problem is always a difficult problem for metallurgists. Comparing with slot tuyere,[6] the porous tuyere may generate more fine bubbles and attach more inclusions into the slag, however, the stirring efficiency is low. The results can be found in Bernd's experiment.[7] Wang[8] established a mathematical model that describe bubble adhesion of inclusions, finding that the inclusions with size of 0.5 to 2 mm are most efficient to remove inclusions smaller than 50 μm; while for the big inclusions, they are mostly removed by bubble wake, which more easily by bubbles larger than 2 mm. Seen from the whole, comparing with porous tuyere, the slot tuyere is more beneficial for alloy mixing, while porous tuyere has advantages in removing inclusions. However, until now, there still lack of tuyeres that can shorten the mixing time and remove more inclusions at the same time. For the purpose of fast mixing and high efficiency of inclusion removement, we come up with an idea that if we use slot–porous matched dual tuyeres in a ladle, it may have significantly different effects from porous–porous or slot–slot tuyeres.

The bubbly flow in the ladle is thought to be multi-scale, fickle and transient.[9–12] For a multiphase system with discrete fine particles and continuous fluids, modeling strategy that track in larger scales while simulate smaller particles without considering their coalescence, breakup and expansion are usually proposed. During the past decades,[13–15] significant developments in the modeling of two-phase flow have occurred since the introduction of the two-fluid model. Fundamentally, the interfacial transport of mass, momentum, and energy are proportional to the interfacial area concentration and driving forces. Since the interfacial area concentration represents the key parameter that links the interaction of the phases, significant attention has been paid towards developing a better understanding of the coalescence and breakup effects.[16–19] Among these studies, the population balance method (PBM) is a well-known method for tracking the size distribution of the dispersed phase and accounting for the breakup and coalescence effects in bubbly flows.[20–23] However, the trajectory of each particle can not be tracked through this approach. By comparison, discrete particle model (DPM) is feasible to track particle flow in the Lagrange approach, which were widely used to simulate bubble movements, inclusion distribution as well as bubble aggregation and breakup,[24–26] however, it still faces extreme challenges for simulating aggregation between particles with different properties, for example, bubbles and inclusions. Thus the modeling for the aggregation-breakup system still remains to be done.

In this work, the main innovations are consisted of three parts: (1) to develop a mathematical model to describe the bubble expansion, as well as aggregation and breakup of particles with different properties; (2) to reveal the effect of bubble expansion on local flow and mixing performance of molten steel; (3) to reveal the characteristics on removing inclusions in a ladle with a special slot–porous matched dual tuyeres. The work lays foundation for the theory of slot–porous tuyeres coupled system.

II. MATHEMATICAL MODELING

A. Mass Conservation Equation

Mass conservation of the three continuous phases (molten steel, slag and air) are satisfied with a single continuity equation:

$$\frac{\partial(\rho_{\mathrm{m}})}{\partial t} + \nabla \cdot (\rho_{\mathrm{m}}\overline{u}_{\mathrm{m}}) = 0 \qquad [1]$$

where $\overline{u}_{\mathrm{m}}$ is the vector of velocity of the mixture of these three continuous phases, t is the time, ρ_{m} is the mixture density, based on the phase volume fractions, the equation can be written as follows:

$$\rho_{\mathrm{m}} = \alpha_{\mathrm{l}}\rho_{\mathrm{l}} + \alpha_{\mathrm{s}}\rho_{\mathrm{s}} + \alpha_{\mathrm{g}}\rho_{\mathrm{g}} \qquad [2]$$

where α_{l} and ρ_{l} are volume fraction and density of molten steel; α_{s} and ρ_{s} are volume fraction and density of liquid slag; α_{g} and ρ_{g} are volume fraction and density of air phase. For simplification, we uses k ($k = l$: steel; $k = s$: slag; $k = g$: air) to represent each phase. Then the α_k is tracked with the following VOF equation:

$$\frac{\partial(\alpha_k)}{\partial t} + \nabla \cdot (\alpha_k \overline{u}_{\mathrm{m}}) = 0 \qquad [3]$$

where ρ_k is the density of k-phase, and α_k is the volume fraction constrained by the equation $\alpha_{\mathrm{l}} + \alpha_{\mathrm{s}} + \alpha_{\mathrm{g}} = 1$.

B. Momentum Conservation Equation

The k-ε model has been widely used in simulating fluid flow, heat and mass transfer as well as bubble movements because of its high efficiency and robustness for simulation. So we adopt this model to calculate the multiphase flow and particle movements in the ladle. The Navier–Stokes (N–S) equation can be written as follows:

$$\frac{\partial(\rho_{\mathrm{m}}\overline{u}_{\mathrm{m}})}{\partial t} + \nabla \cdot (\rho_{\mathrm{m}}\overline{u}_{\mathrm{m}}\overline{u}_{\mathrm{m}}) = -\nabla\overline{P} + \nabla$$
$$\cdot \left[\mu_{\mathrm{effect,m}}(\nabla\overline{u}_{\mathrm{m}} + \nabla\overline{u}_{\mathrm{m}}^{\mathrm{T}})\right]$$
$$+ \rho_{\mathrm{m}}g + \frac{6}{\pi d_{\mathrm{p}}^{3}} \cdot F + F_{\mathrm{T}}$$
$$[4]$$

Here, the term $\overline{P}$ is the static pressure, F is the particle forces acted on steel, $\mu_{\mathrm{effect,m}} = \mu_{\mathrm{m}} + \mu_{\mathrm{t}}$ is the effective viscosity of mixture phase. Term μ_{m} is the molecular viscosity of mixture phase, d_{p} is the diameter of argon bubble, and μ_{t} is the turbulent viscosity of mixture phase. They are all averaged by the volume fraction of each phase in VOF approach. The surface tension force F_{T} in Eq. [4] is calculated by:

$$F_{\mathrm{T}} = \begin{cases} 2\sigma_{\mathrm{s-l}}\rho_{\mathrm{m}}C_{\mathrm{s-l}}\nabla\alpha_k/(\rho_{\mathrm{l}}+\rho_{\mathrm{s}}) & \text{for: slag(s)-metal(l)\,interface} \\ 2\sigma_{\mathrm{s-g}}\rho_{\mathrm{m}}C_{\mathrm{s-g}}\nabla\alpha_k/(\rho_{\mathrm{s}}+\rho_{\mathrm{g}}) & \text{for: slag(s)-air(g)\,interface} \end{cases}$$
$$[5]$$

where $\sigma_{\mathrm{s-l}}$ and $\sigma_{\mathrm{s-g}}$ are the surface tension coefficient for slag–metal interface and slag–air interface, $C_{\mathrm{s-l}}$ and $C_{\mathrm{s-g}}$ are the curvature of the slag–metal and slag–air interface.

The calculation for kinetic energy and turbulence intensity in multiphase flow are shown below:

$$\frac{\partial(\rho_{\mathrm{m}}k)}{\partial t} + \nabla \cdot (\rho_{\mathrm{m}}k\overline{u}_{\mathrm{m}}) = \nabla \cdot \left(\frac{\mu_k}{\sigma_k}\mu_{\mathrm{effect,m}}\nabla k\right) + 2\mu_t S_{ij}$$
$$\cdot S_{ij} - \rho_{\mathrm{m}}\varepsilon$$
$$[6]$$

$$\frac{\partial(\rho_{\mathrm{m}}\varepsilon)}{\partial t} + \nabla \cdot (\rho_{\mathrm{m}}\varepsilon\overline{u}_{\mathrm{m}}) = \nabla \cdot \left(\alpha_\varepsilon\frac{\mu_{\mathrm{effect,m}}}{\sigma_\varepsilon}\nabla\varepsilon\right)$$
$$+ C_{1\varepsilon}\frac{\varepsilon}{k}2\mu_t S_{ij} \cdot S_{ij} - C_{2\varepsilon}\rho\frac{\varepsilon^2}{k} \quad [7]$$

where $\sigma_k = 1$, $\sigma_\varepsilon = 1.3$, $C_{1\varepsilon} = 1.44$, $C_{2\varepsilon} = 1.92$. Other variables can be found in previous equations.

C. Bubble Transportation Model

In this work, the movements of discrete bubbles are tracked through Lagrangian approach. To simulate the effect of bubbles on fluid flow, the interactions between the continuous phases and discrete bubbles were two-way coupling. For instance, the motion of particles can be simulated by integrating the force balance equation for each particle, which can be written as:

$$m_{\mathrm{p}}\frac{d\overline{u}_{\mathrm{p}}}{dt} = F \qquad [8]$$

where $\overline{u}_{\mathrm{p}}$ and $\overline{m}_{\mathrm{p}}$ represent the velocity and mass of bubbles, and F represents total forces acted on bubbles, which can be expressed as:

$$F = F_{\mathrm{g}} + F_{\mathrm{b}} + F_{\mathrm{p}} + F_{\mathrm{d}} + F_{\mathrm{l}} + F_{\mathrm{v-m}} \qquad [9]$$

The terms on the right side of Eq. [9] are gravitational force, buoyancy force, pressure gradient force, drag force, lift force, virtual mass force. The forces acted on the bubbles and the expressions for the terms on right side of the equations can be found in our previous works.[27,28]

Bubbles are injected into the ladle at room temperature and expand in molten steel. The bubble density in the molten steel can be calculated through ideal gas law:

$$P = \rho_{p,ar}R_g T \qquad [10]$$

Here, the bubble density ρ_p at 20 °C is 1.78 kg/m^3. T is steel temperature.

In the Lagrange framework, the density of two particles after coalescence is computed as the weighted average of volume fraction for each phase:

$$\rho_p = \frac{V_{p,ar}\rho_{p,ar} + V_{p,inc}\rho_{p,inc}}{V_{p,ar} + V_{p,inc}} \qquad [11]$$

D. *Bubble Transport Model*

The bubble size model is controlled by material properties and turbulence. The equilibrium diameter is the diameter that it is achieved if a bubble resides long enough at the same flow conditions, which can be written as:

$$d_p^{eq} = C_1 \beta^{0.5} \frac{\left(\sigma/\rho_m\right)^{0.6}}{\varepsilon^{0.4}} \left(\frac{\mu_p}{\mu_m}\right)^{0.25} + C_2 \qquad [12]$$

where the coefficients C_1 and C_2 are 4 and 100 μm, respectively. β is volume fraction of the particles in a geometry cell. The relaxation time is the time that is needed for bubble to reach the equilibrium diameter. The mean bubble diameter will be driven to its equilibrium diameter during a timeframe given by the relaxation time.

The relaxation time is restricted by the turbulent microscale that represents the smallest timescale in a turbulent flow. The relaxation time τ_{rel} is given:

$$\tau_{rel} = \begin{cases} \tau_B & \text{Breakup} \\ \tau_C & \text{Coalescence} \end{cases} \qquad [13]$$

$$\tau_{rel} = |\tau_{rel}, \tau_k|_{max} \qquad [14]$$

where τ_k is the turbulent microscale which is determined by the following equation:

$$\tau_k = 6\sqrt{\frac{v}{\varepsilon}} \qquad [15]$$

where v is the kinematic viscosity of the fluid. The relaxation times for breakup τ_B and coalescence time scale τ_C are determined by:

$$\tau_B = d_b^{\frac{2}{3}} \varepsilon^{-\frac{1}{3}} \qquad [16]$$

$$\tau_C = \frac{d_b}{0.2 \times 6 \times \sqrt{\beta k}} \qquad [17]$$

When the model is implemented in code, if a bubble is bigger than d_p^{eq} then the bubble's breakup occurs otherwise the coalescence will occur. τ_B or τ_C will be obtained, the relaxation time is restricted by turbulent microscale that represents the smallest timescale in turbulent flow.[29,30] Bubble size is restricted to have a diameter size above 0.0001 m. The fraction of the bubble is also restricted to be below 1×10^{-6}. Then the particle diameter after coalescence and breakup can be written as:

$$\begin{cases} d_p' = \left(d_p + d_{cr} \times dt/\tau_B\right)/(1.0 + dt/\tau_B) & \textit{If} \text{ breakup} \\ d_p' = \left(d_p + d_{cr} \times dt/\tau_C\right)/(1.0 + dt/\tau_C) & \textit{If} \text{ coalescence} \end{cases} \qquad [18]$$

Figure 2 shows the particle transport with different conditions. First, when the bubbles and inclusions are aggregated, a new particle is formed with the averaged density of volume fraction for each phase, then the mass, velocity and density can be written as:

$$\begin{cases} m_p = m_1 + m_2 \\ \overline{u}_p = \dfrac{m_1 \overline{u}_{p,1} + m_2 \overline{u}_{p,1}}{m_1 + m_2} \\ \rho_p = \dfrac{m_1 + m_2}{V_1 + V_2} \end{cases} \qquad [19]$$

When two bubbles are aggregated, they form a new particle, then the mass, velocity and density can be written as:

$$\begin{cases} m_p = m_1 + m_2 \\ \overline{u}_p = \dfrac{m_1 \overline{u}_{p,1} + m_2 \overline{u}_{p,1}}{m_1 + m_2} \\ \rho_p = \text{Constant} \end{cases} \qquad [20]$$

Assuming that after breakup two bubbles are formed with the same diameter and velocity, then the mass, velocity and density can be written as:

$$\begin{cases} m_1 = m_2 = 1/2 m_p \\ \rho_p = \text{Constant} \\ u_p = \text{Constant} \end{cases} \qquad [21]$$

In these equations, m_1 and m_2 are previous mass for two particles, $\overline{u}_{p,1}$ and $\overline{u}_{p,2}$ are previous velocity for two particles, and $\overline{u}_p$ is velocity after coalescence or breakup. The aggregation of bubble itself and inclusions, as well as the mass and momentum exchanges are shown in Figure 2.

E. *Species Transport Model*

In order to track the transportation of metallic elements driven by the flow field of liquid steel, a virtual liquid is defined with the assumption that the physical properties are equal to the liquid steel. The transportation equation can be written as follows:

$$\frac{\partial(\rho_m c)}{\partial t} + \frac{\partial\left(\rho_m u_{m,j} c\right)}{\partial x_j} = \frac{\partial}{\partial x_j}\left[\left(\frac{\mu_m}{S_{C1}} + \frac{\mu_t}{S_{Ct}}\right)\frac{\partial c}{\partial x_j}\right] \qquad [22]$$

where c is the concentration of solution, μ_m and μ_t are molecule viscosity and turbulent viscosity, $S_{Ct} = 0.1$ is laminar Schmidt number, $S_{C1} = \mu_m/(\rho_m D_m)$ is turbulent Schmidt number, D_m is solution diffusion coefficient.

F. *Boundary Condition and Numerical Details*

Based on similarity principle, a 1:7 scale experimental model is used to visualize the flow-related phenomena in a ladle, just as shown in Figure 3. The system is composed of water model, tuyeres, gas pipe and air compressor. The gas is injected from the bottom of the ladle through an air compressor at the pressure of 0.4
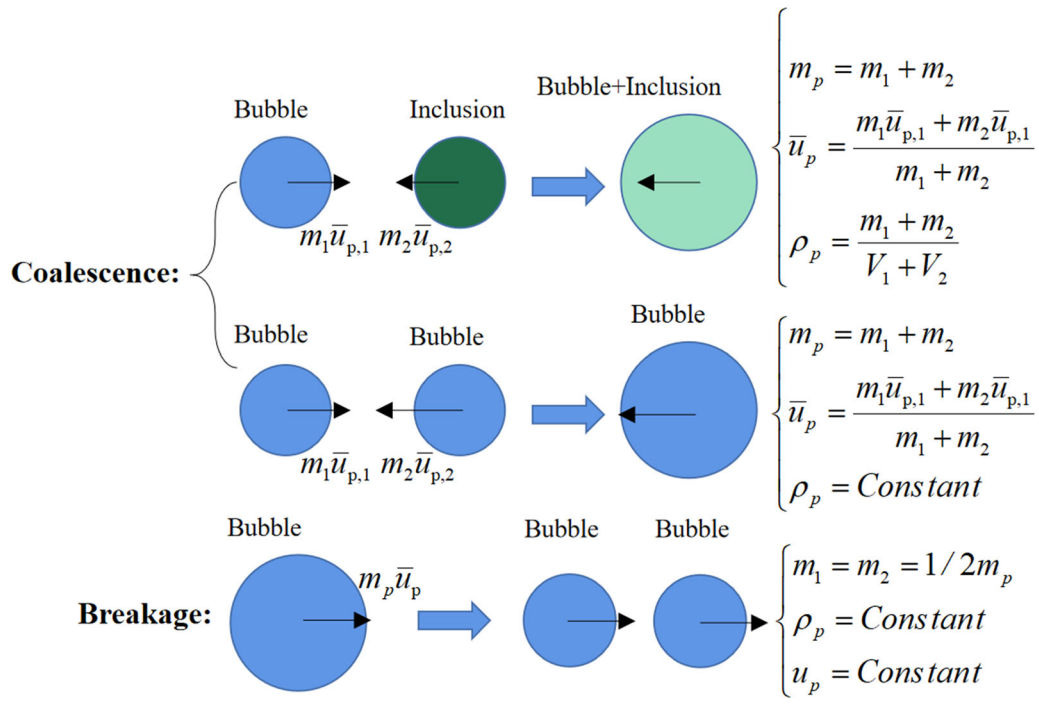
$$\begin{cases} m_p = m_1 + m_2 \\ \bar{u}_p = \dfrac{m_1 \bar{u}_{p,1} + m_2 \bar{u}_{p,1}}{m_1 + m_2} \\ \rho_p = \dfrac{m_1 + m_2}{V_1 + V_2} \end{cases}$$

$$\begin{cases} m_p = m_1 + m_2 \\ \bar{u}_p = \dfrac{m_1 \bar{u}_{p,1} + m_2 \bar{u}_{p,1}}{m_1 + m_2} \\ \rho_p = Cons\,tant \end{cases}$$

$$\begin{cases} m_1 = m_2 = 1/2 m_p \\ \rho_p = Cons\,tant \\ u_p = Cons\,tant \end{cases}$$

Fig. 2—Aggregation and breakup of particles in a bubble-inclusion coexisting system.
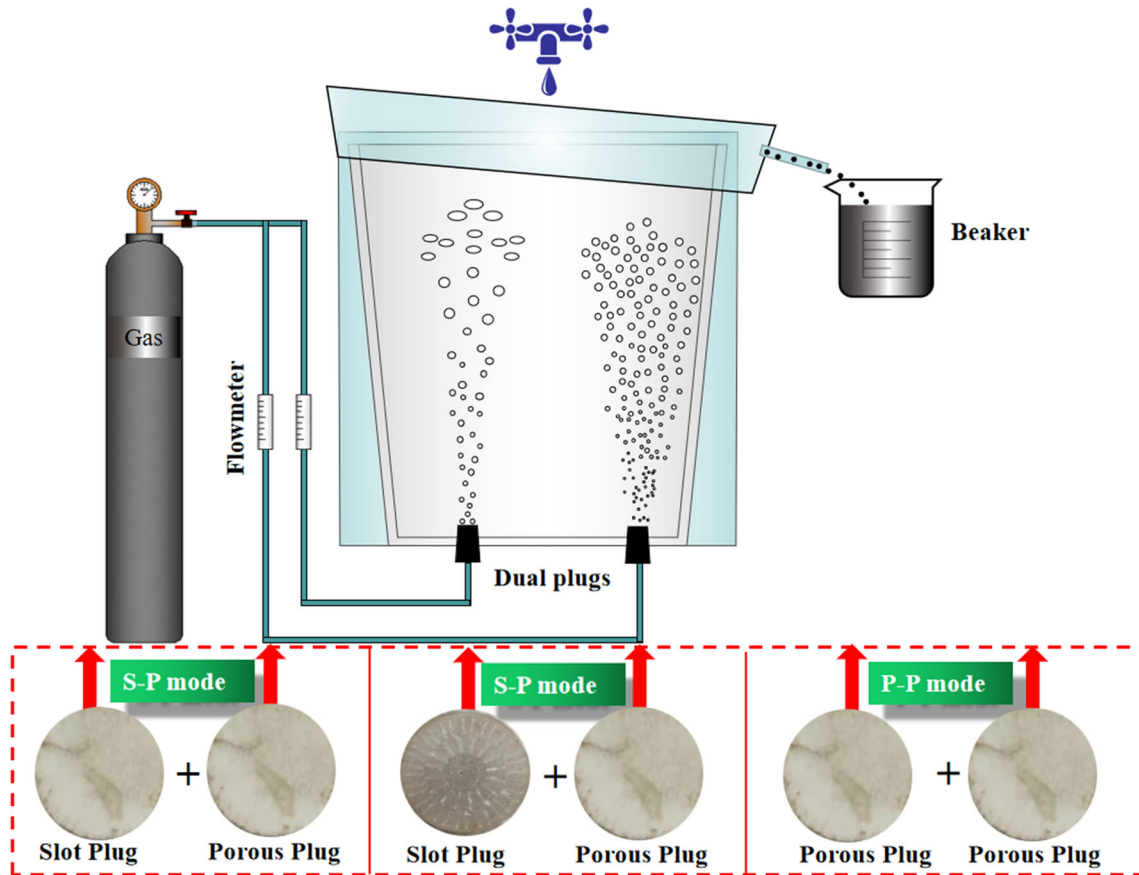
Fig. 3—Configuration of water model experiment.
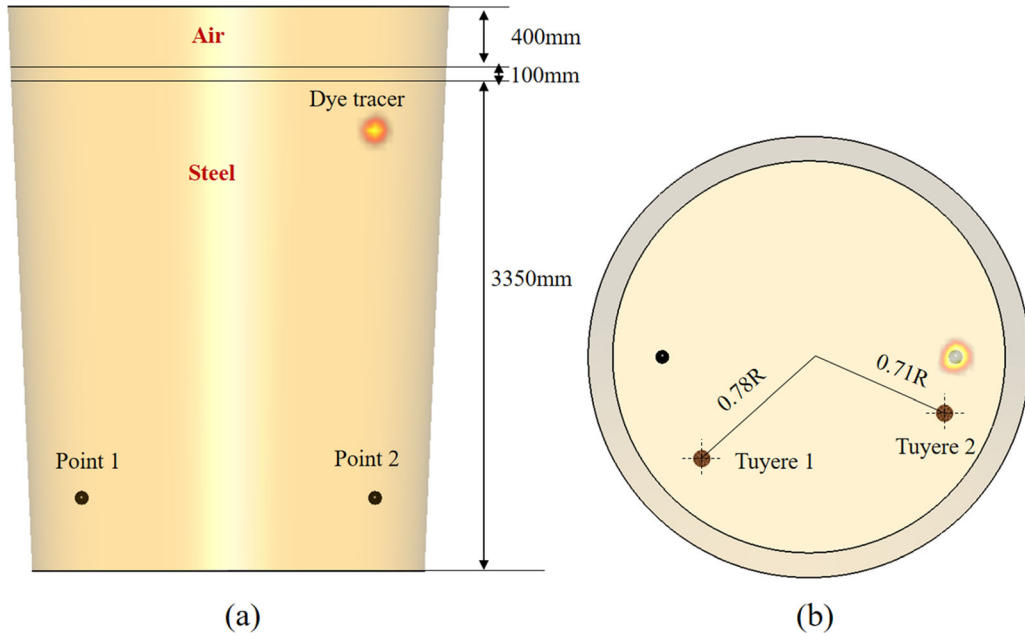
Fig. 4—Geometry and boundary conditions for the full size model: (*a*) isometric view, (*b*) top view.

MPa; A water tap is mounted above the model and constantly supply fluid water at a fixed flow rate. Then the inclusions near free-surface would be pushed out by the overflow and allocated into the beaker through a thin plastic channel. The removed fraction of inclusions into the container can be read through the label carved on the beaker. Three kinds of tuyere matches are investigated: The first match is called S–S mode, which is composed of two slot tuyeres; The second match is named S–P mode which is composed of one slot and one porous tuyeres; The last match is composed of two porous slags (P–P mode). The removed fraction of inclusion is monitored every minute, and the monitored time is 10 minutes. The dioctyl phthalate is used to substitute inclusions in the ladle because the dioctyl phthalate is a liquid material that can aggregate and breakup in the water. The percentage of inclusion removal within every minute can be obtained through this model.

Based on the ideal gas law, the gas in the standard state and practical ladle is quite different, the relationship between the two state can be written as:

$$\frac{\rho_{l,p}gH_p + p_0}{p_0} = \frac{\rho_{g,p}T}{\rho_{g,0} \cdot 273.15} \qquad [23]$$

where the depth of molten steel $H_p = 3350$ mm, standard atmospheric pressure $p_0 = 101325 P_a$, argon density at standard state $\rho_{g,0} = 1.786$ kg/m^3, density of molten steel $\rho_{l,p} = 7100$ kg/m^3, temperature of molten steel is $T = 1831.15K$. The density of gas density is $\rho_{g,p} = 0.879$ kg/m^3.

Considering bubbles expansion after injected into the steel, the argon flow rate is calculated as:

$$Q_{g,p} = \frac{\rho_{g,0}}{\rho_{g,p}}Q_{g,0} = 2.031\ Q_{g,0} \qquad [24]$$

where $\rho_{g,0}$ is density of argon at 0 °C. The Froude number in the real ladle and experiment should be equal, which can be written as:

$$\frac{\rho_{g,m}u_m^2}{\rho_{l,m}gH_m} = \frac{\rho_{g,p}u_p^2}{\rho_{l,p}gH_p} \qquad [25]$$

The injection velocity of gas is calculated as:

$$u = \frac{4Q}{\pi d^2} \qquad [26]$$

Based on the Eqs. [25] and [26], the following equation can be obtained:

$$\frac{Q_{g,m}}{Q_{g,p}} = \sqrt{\frac{\rho_{g,p} \cdot d_m^4 \cdot H_m \cdot \rho_{l,m}}{\rho_{l,p} \cdot d_p^4 \cdot H_p \cdot \rho_{g,m}}} = 0.00251 \qquad [27]$$

where water density $\rho_{l,m} = 1000$ kg/m^3, and air density $\rho_{g,m} = 1.171$ kg/m^3.

Through all the equations stated above, the relationship of argon flow rate between experiment and real ladle can be obtained:

$$\begin{aligned} Q_{g,m} &= 0.00251Q_{g,p} = 0.00251 \times 2.031 \times Q_{g,0} \\ &= 0.0051\ Q_{g,0} \end{aligned} \qquad [28]$$

The mixture of vacuum pump oil and kerosene is substituted as the slag. The viscosity should obey:

$$\frac{v_{slag}}{v_{steel}} = \frac{v_{oil}}{v_{water}} \qquad [29]$$

In this equation, v_{steel} and v_{water} are viscosity of water and molten steel, m^2/s.

Figure 4 shows the computational domain with two tuyeres inserted at the bottom of the ladle. One of the tuyeres is located on the 0.78 radius of the ladle bottom, and the other one is located on the 0.71 radius of the bottom. The angle between two tuyeres is 114 deg. The free surface is 400 mm distance from the ladle top. The slag layer thickness is 100 mm. What's more, in order to investigate fluid mixing behavior under different tuyere matches, we monitored two typical points distributed symmetrically along left and right side of the ladle, just as shown in Figure 4(a). The mixing time is defined as the time when the concentration difference between two points is less than 5 pct. The dye tracer is fed above Point 2, near the slag–metal interface.

Many previous works[31–33] have modeled the dynamic characteristics for bubble collision, aggregation and breakup. Validations are made through water model experiment. It's widely believed that bubble size changes have important effects on momentum exchange, fluid mixing and chemical reactions. For example, bubble would expand and accelerate when it rises to the top, resulting in decrease in density and increase in velocity. But until now, few works has been done to explore this phenomenon and its effect on the particle movements and fluid mixing behavior. As a result, the refining effect is still hard to control at present, it's quite necessary to investigate the complex bubbly driven flow inside the ladle.

Table I. Geometry and Material Properties

Parameters	Real Ladle	Water Model (Scale 1:7)
Gas Flow Rate, NL/min	150 + 150	0.765 + 0.765
Tuyere Angle deg	114 deg	114 deg
Dynamic Viscosity of Steel, kg/(m·s)	0.0051	0.001
Dynamic Viscosity of Air, kg/(m·s)	1.79×10^{-5}	1.79×10^{-5}
Density of Dioctyl Phthalate, kg/(m³)	2800	900
Radius of Ladle Bottom, mm	2717	388
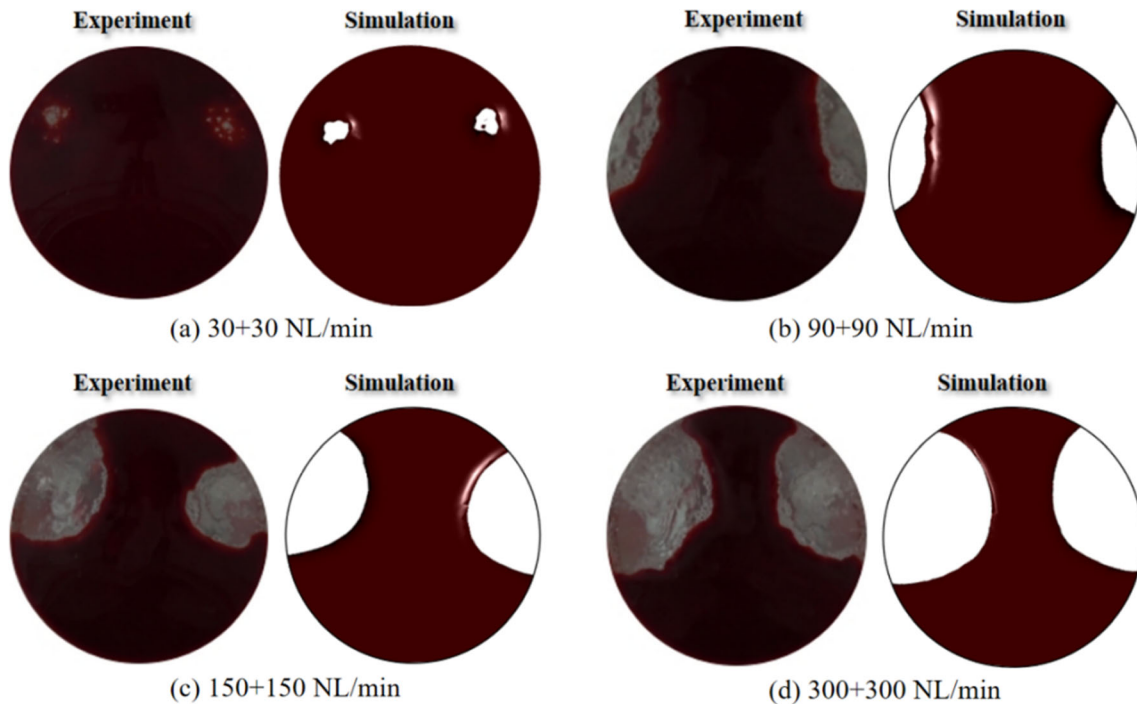
Fig. 5—Comparison of naked eyes between water experiment and simulation results with different flow rate: (a) 30 + 30 NL/min, (b) 90 + 90 NL/min, (c) 150 + 150 NL/min, (d) 300 + 300 NL/min.
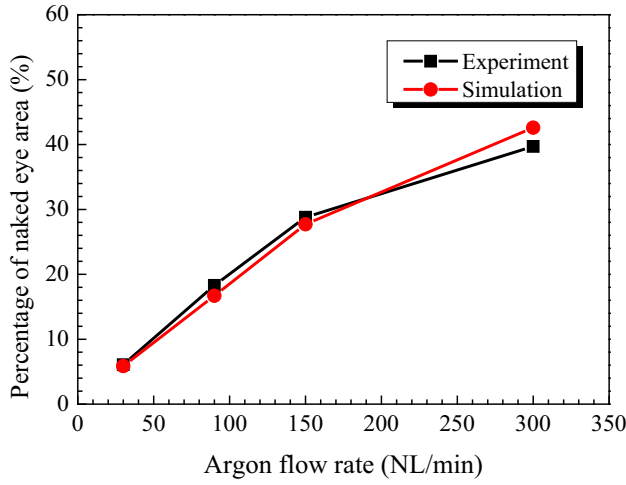
Fig. 6—Comparison of naked eyes through between experiment and simulation.

Fig. 7—Transient percentage of inclusion removement with different modes.

Just as stated above, bubble would expand when it rises to the top. The reason for this phenomenon is because the ambient pressure would decrease in this way. The bubble volume at different immersion height can be written as:

$$\rho_p = \frac{P_0 + \rho_m g H}{R_g T} \quad [30]$$

where H represents the distance from free surface to bubble location. Through this equation, the expansion of bubbles can be solved.

The initial bubble size distribution is assumed to obey Romin–Rosin law, which can be described as follows:

$$Y_d = e^{-(d/d_m)^n} \quad [31]$$

Here, the variable Y_d is the mass fraction of bubbles whose diameters are greater than d. For the bubbles injected from a slot tuyere, the minimum and maximum bubble diameter are 5 and 15 mm, respectively, and the averaged bubble diameter $d_m = 8$ mm; By comparison, for the bubbles injected from a porous tuyere, the minimum and maximum bubble diameter are 2 and 5 mm, respectively, and the averaged bubble diameter $d_m = 3$ mm, and the spread parameter $n = 1.1$. Parameters used in this study are summarized in Table I.

III. RESULTS AND DISCUSSION

A. *Validation for Mathematical Model*

Water model experiments are carried out to validate the mathematical model. It should be noticed that to make comparisons, the argon flow rate illustrated in the water model represents the value in practical ladle. It can be seen from Figure 5(a) that when the argon flow rate is low (30 + 30 NL/min), the slag eyes doesn't contact with the ladle wall, and the area is quite small. However, after increasing to 90 + 90 NL/min, the naked eyes are larger and start to contact the wall. This may diminish the service life because of refractory erosion.

When the flow rate continues to grow, naked eyes' region become larger and larger. Naked eyes' exact area are estimated using Image J package, just as shown in Figure 6. Easily seen, Simulation results are similar with experimental results, indicating that the mathematical model in this work is reliable.

Figure 7 illustrates inclusion's removal with different tuyere matches. It shows that even though the kinetic energy in S–S mode is high, the inclusions removal rate was low comparing with other modes. But after replacing one of the slot tuyere with porous tuyere, the inclusion removal rate has significantly raised. The reason for this phenomenon, on the one hand, is because more small-scale bubbles were generated to attach the inclusions to float up, on the other hand, is because the small bubbles may distribute more uniformly under the effect of slot tuyere. When the two tuyeres are all substituted by porous tuyeres (P–P mode), the inclusion removal rate is marginally reduced, but still more excellent than S–S mode. This implies that the utilization of porous tuyeres exhibits a considerable impact on inclusion's removal behavior.

B. *Coalescence and Breakup of Bubbles and Attachment of Inclusions*

Figure 8 displays the breakup and coalescence of bubbles in molten steel. In the simulation work, the geometry of the ladle is corresponding to the actual ladle so as to reveal the flow-related phenomenon during secondary refining process. At the beginning of the time, two bubbles aggregated and 0.01 second later, one of them take small bubbles in and becomes a larger one. Furthermore, in a similar way larger bubbles may also split into some smaller ones, just as shown in Figure 8(b). Due to the decreasing of hydraulic pressure the bubbles would expand when rising to the top. This explains why the bubbles near the top are much larger than that near the bottom. Due to the bubble expansion, the density of bubbles are mostly decreases to 0.3 to 0.8 kg/m³. The
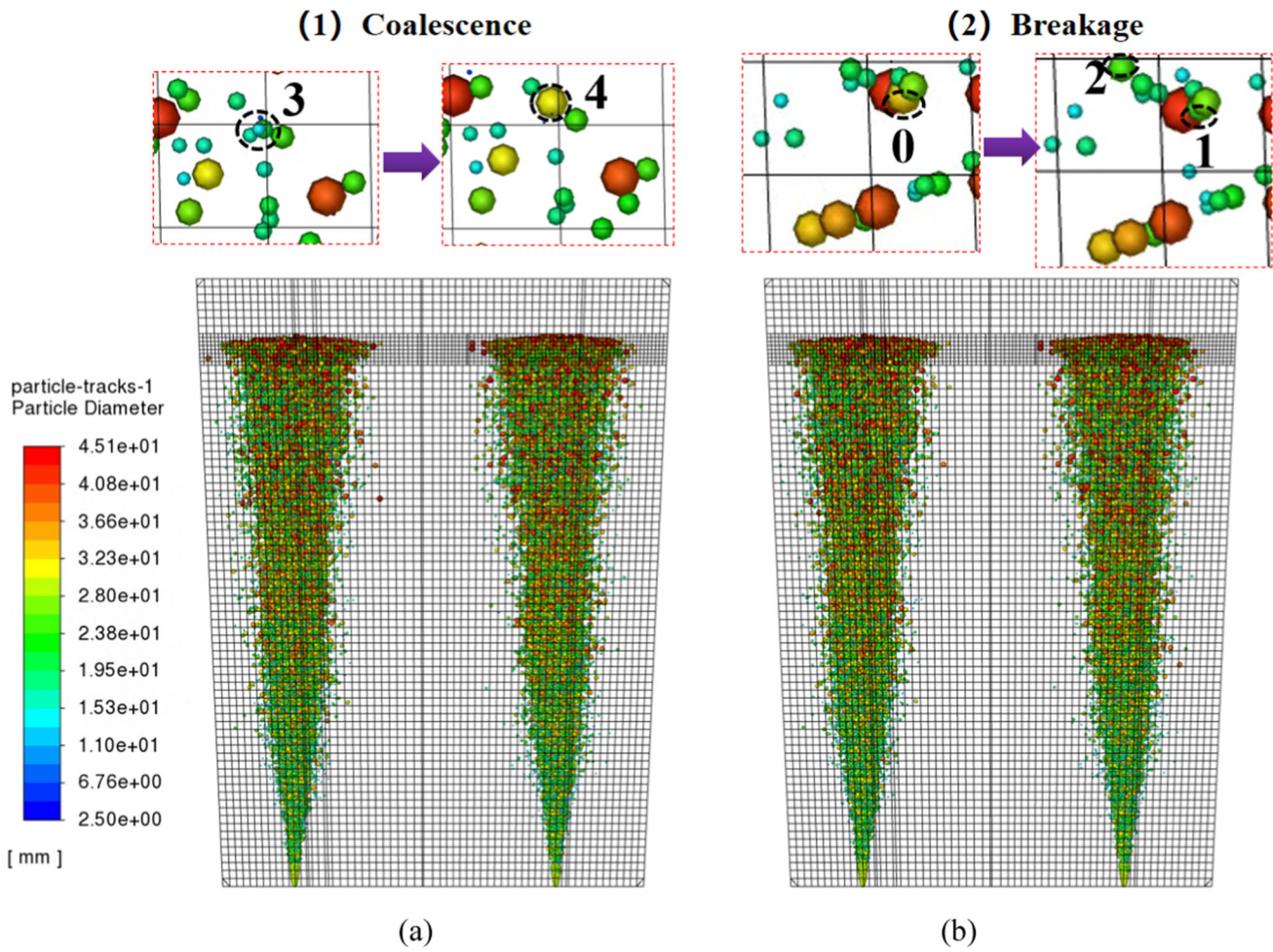
Fig. 8—Prediction of bubble diameter distribution and coalescence/breakup process: (*a*) *t* = 200 s, (*b*) *t* = 200.01 s.
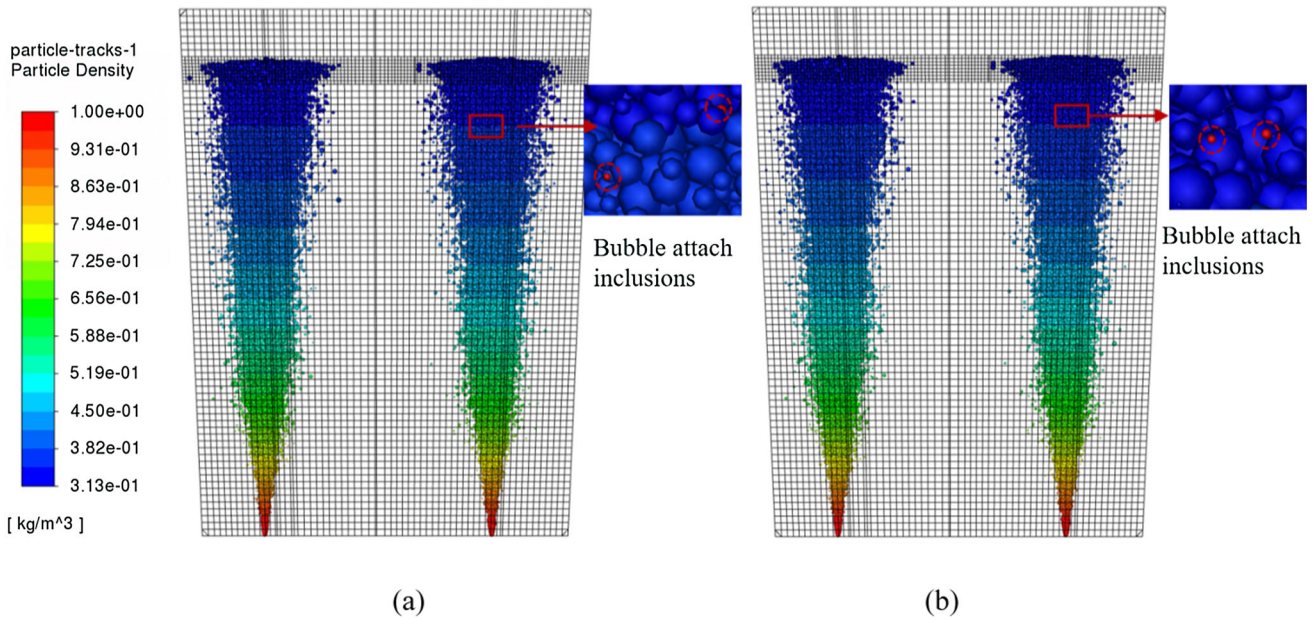

Fig. 9—Prediction of bubble density distribution and coalescence/breakup process: (*a*) *t* = 200 s, (*b*) *t* = 200.01 s.
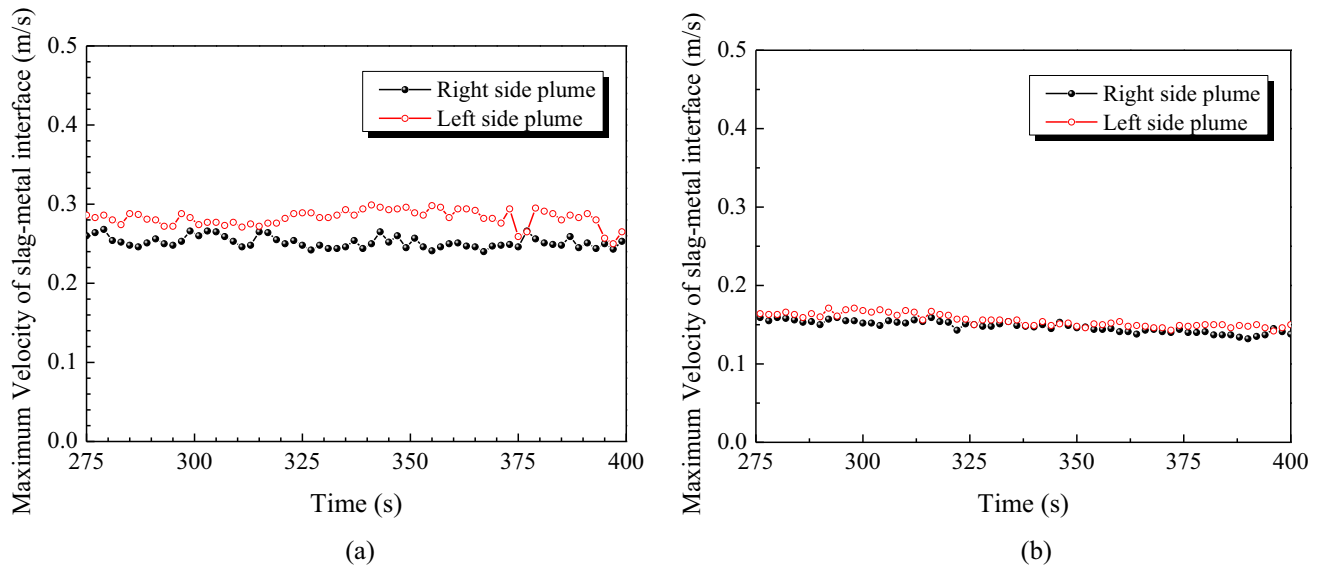
Fig. 10—Comparison of maximum velocity on the slag–metal interface with (*a*) consideration of bubble expansion and (*b*) ignorance of bubble expansion.
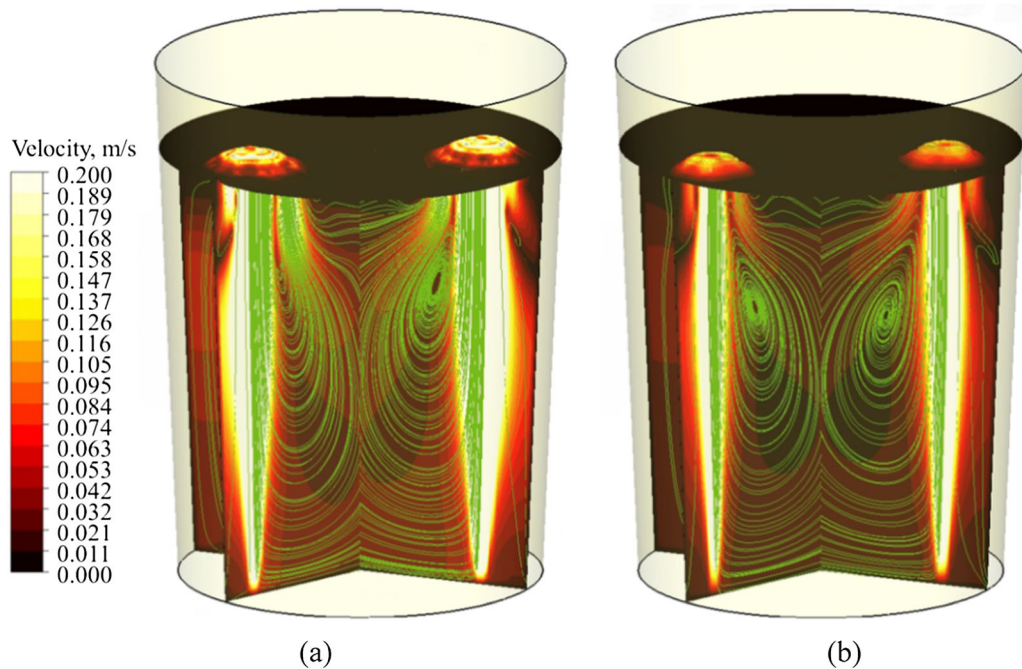

Fig. 11—Comparison of velocity distribution on the slag–metal interface with (*a*) consideration of bubble expansion and (*b*) ignorance of bubble expansion.

plume zone is presented as a V-like shape since the bubbles involve surrounding liquid, forming a circulation inside the ladle. What's more, bubble density rises with distance from the bottom to the ladle's top due to bubble expansion, just as shown in Figure 9. And they may sometimes attach surrounding inclusions, which increase bubble densities notably, just as depicted in the magnified zone. All these phenomenon are vividly revealed by this mathematical model.

C. *Effect of Bubble Expansion on the Flow Field and Inclusion Transport*

A lot of researchers[34–36] have mentioned that in a bubbly driven tube, bubble size' differences are mostly caused by two aspects: one is breakup and aggregation, the other one is expansion. In a ladle with two tuyeres, just as shown in Figure 4(b), the tuyere at right side of ladle is located at the 0.71 radius of the bottom, and the tuyere at the left side is located at the 0.78 radius. In the
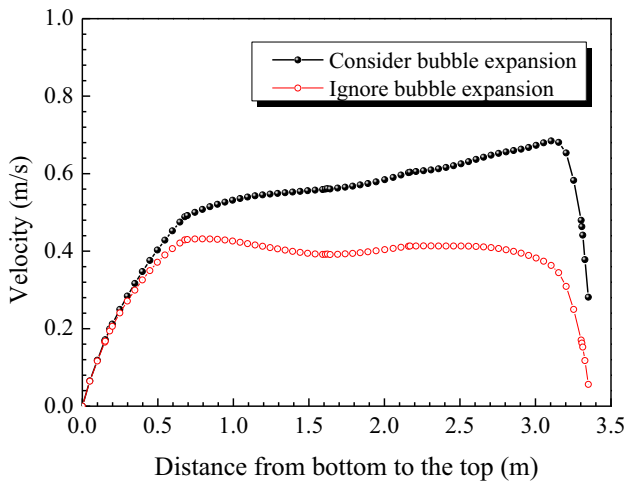
Fig. 12—Comparison of velocity on the axis of plume zone.

following paragraph, two plume zones' axises were monitored at vertical directions. Figure 10 shows that because the tuyere on the left side is close to the wall, the maximum velocity on slag–metal interface's left side is higher than that in the right side. This is why the area of left slag eye is larger than the right slag eye, just as shown in water model experiment in Figure 5. Without considering bubble expansion, the maximum velocity is 0.171 m/s (see Figure 10(a)), while taking this into account, the maximum velocity rises to 0.299 m/s (see Figure 10(b)). Under such circumstance, the velocity of slag–metal interface rises a lot, and the cores of vortices are getting closer to the top, just as exhibited in Figure 11.

Figure 12 shows the velocity magnitude on plume zone's axises. Due to expansion, bubbles are accelerated continuously when floating to the top, as a result, the velocity increases with distance from bottom to the top until they touch the slag–metal interface. Then the

(a)

(b)
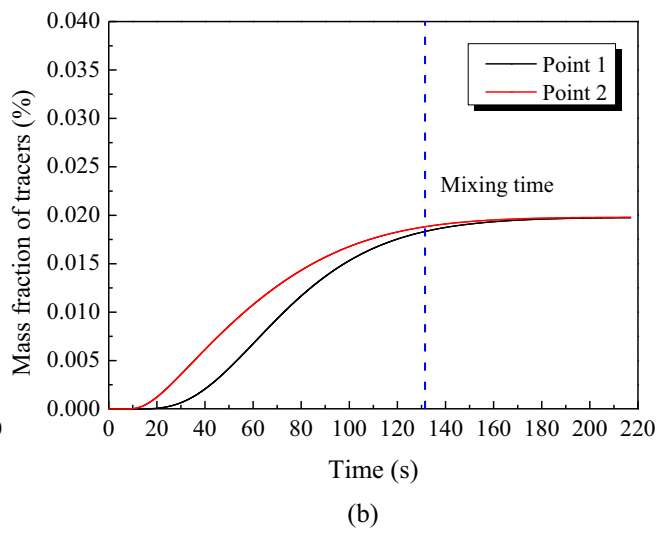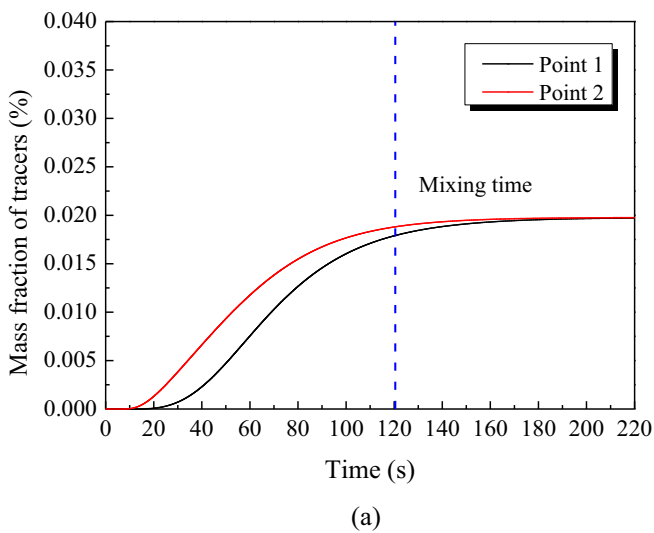
Fig.13—Effect of bubble expansion on the mixing behavior: (a) consider expansion, (b) ignore expansion.

(a)

(b)
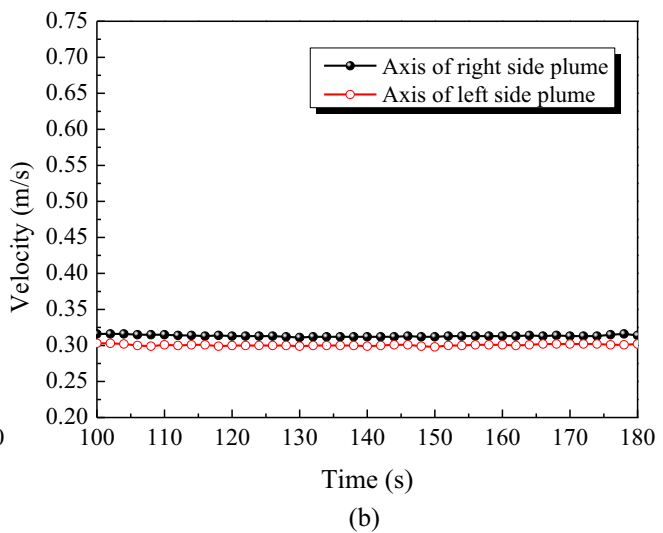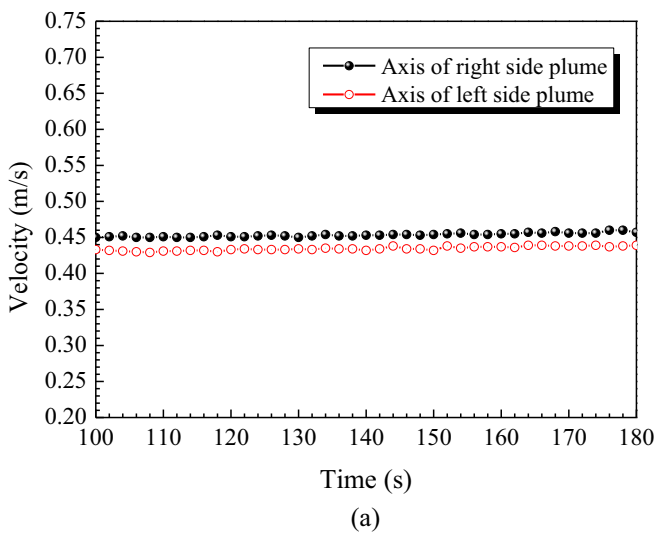
Fig. 14—Comparison of velocity magnitude at axis of plume: (a) consider bubble expansion; (b) ignore bubble expansion.
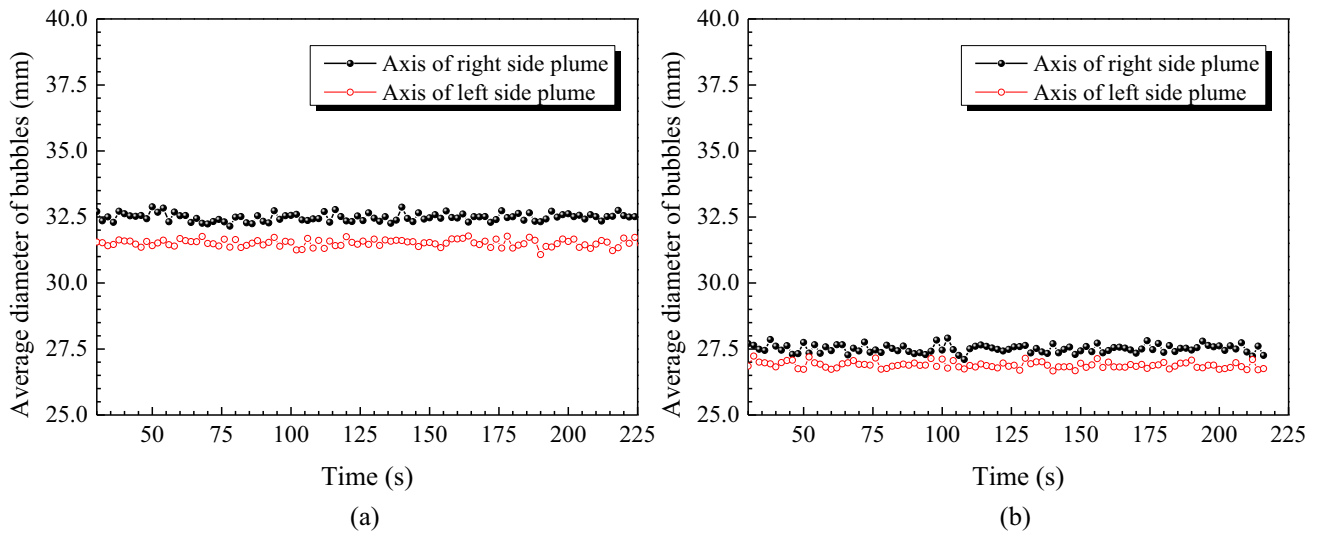
Fig. 15—Comparison of bubble diameters at axis of plume zone: (*a*) consider bubble expansion; (*b*) ignore bubble expansion.
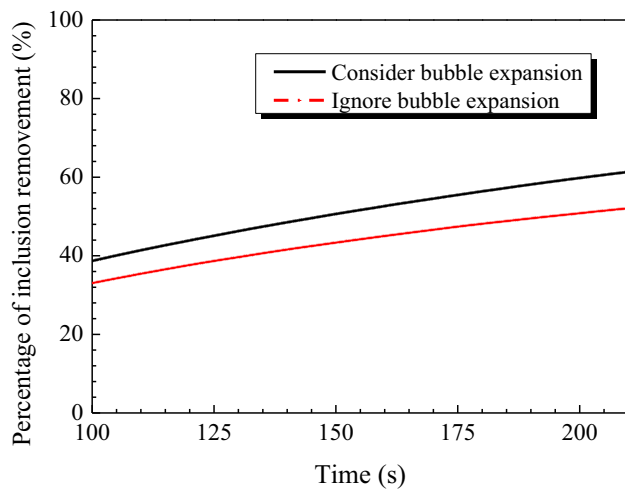

Fig. 16—Comparison of Inclusion removement with/without considering of bubble expansion.

velocity decreases rapidly before escaping from the slag layer. However, if bubble expansion is ignored during numerical simulation, the bubbles are firstly accelerated due to buoyancy force, then they reach a quasi-steady state after rising 0.7 m, and then gradually decreases when floating to the top. This is not consistent with common sense, therefore the bubble expansion is not suggested to be ignored during numerical simulation.
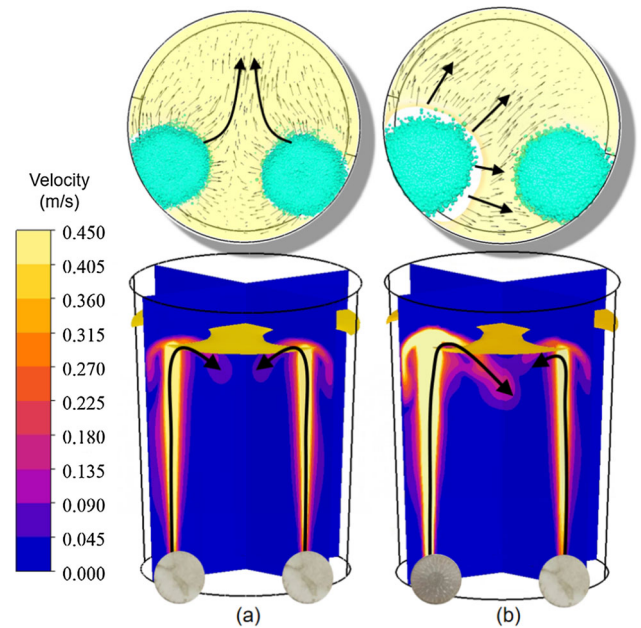
Fig. 17—Prediction of flow field through different modes: (*a*) S–S mode, (*b*) S–P mode.

Since velocity is decreased without considering expansion, the mixing time is much more delayed, just as shown in Figures 13(a) and (b). The mixing time when considering bubble expansion is 120.45 seconds, while the mixing time is 9.2 pct delayed without considering bubble expansion, reaching 131.5 seconds.
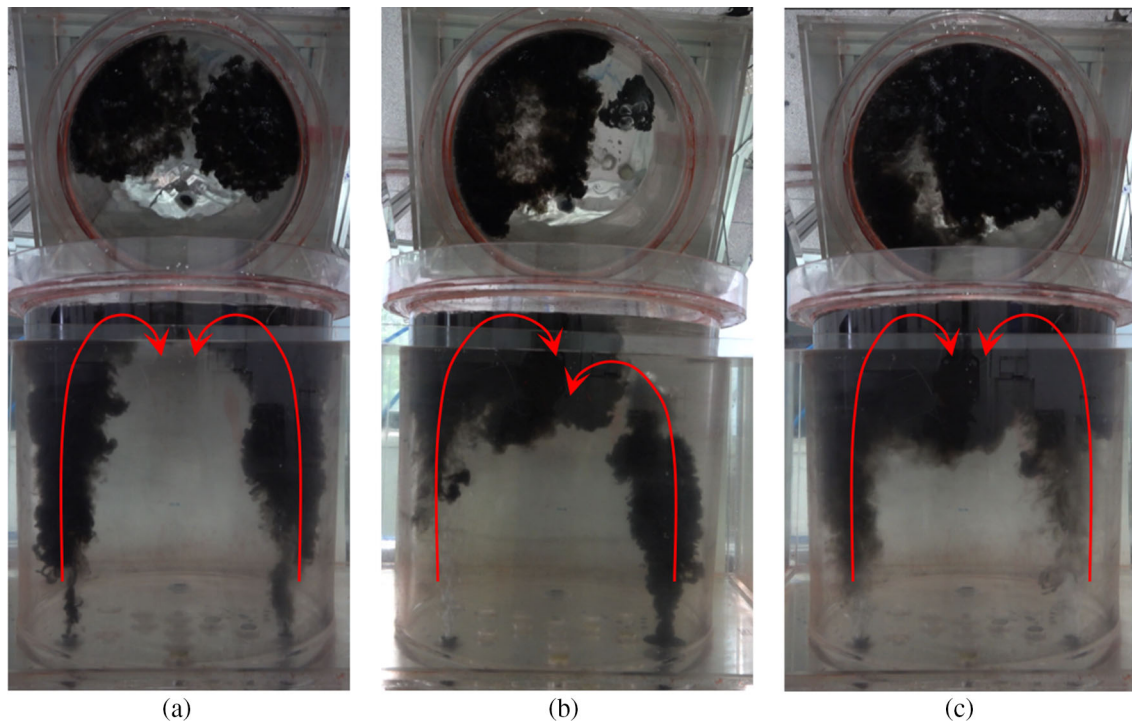
Fig. 18—Dye tracer distribution with different injection modes: (*a*) S–S mode, (*b*) S–P mode, (*c*) P–P mode.

In order to evaluate bubble expansion on the flow field, we analyzed the averaged velocity on plume zones' axises under S–S mode. The result is shown in Figure 14. According to Figure 14(a), owning to the tuyere on the left side is approximate to the wall, the averaged velocity on the left side is lower than that in the right side. The reason is that the liquid steel is constricted by the static wall. When considering bubble expansion, the averaged velocity on plume zones' axises are significantly decreased. The reason for this phenomenon is because without considering bubble expansion, the averaged volume of bubble would be evidently underestimated, just as shown in Figure 15.

Furthermore, in order to evaluate effect of bubble expansion on distribution of bubble diameter, the transient averaged diameters on plume zones' axises are shown in Figure 15. As the velocity near the left plume zone is low, the bubbles especially the smaller ones are not easy to float up, as a result, averaged bubble diameters are smaller than that in the right side. Considering bubble expansion, the diameters on both sides are significantly larger than that bubble expansion is ignored.

Figure 16 illustrates the effect of bubble expansion on removal of inclusions. Due to the high velocity field owing to bubble expansion, the velocity of particle is also increased. As a result, the inclusion removement ratio is increased. Over all, the bubble expansion could significantly affect the fluid flow, mixing, and inclusion

removements during ladle refining. Therefore, the bubble expansion is not suggested to be ignored in simulation.

D. *Effect of Tuyere Matches on the Flow Field and Inclusion Transport*

Different tuyeres have different metallurgical effects because bubble size distributions are quite different. In the early years, porous tuyeres are commonly used in ladle because it is easily designed and fabricated, however, the alloys are too difficult to diffuse into the steel since the stirring energy is low. The problem has been overcome since slot tuyeres are successfully designed. Until today, most companies still adopt this kind of tuyere, especially with two sites. However, the inclusion in the steel is hard to be removed because the fluctuation of slag layer is excessively intensified.

Different from previous works, we proposed a new collection of tuyeres called slot-porous matched dual tuyeres. Figure 17 predicts flow field as well as slag eyes under different conditions. According to Figure 17(a), the flow field in the conventional S–S mode is almost symmetry and uniform, while after using S–P mode, the flow field becomes asymmetry and non-uniform, just as displayed in Figure 17(b). This implies that the S–P mode significantly changed the flow field in ladle. As bubble diameter along slot tuyere is larger than that in the porous tuyere side, then the velocity along the slot
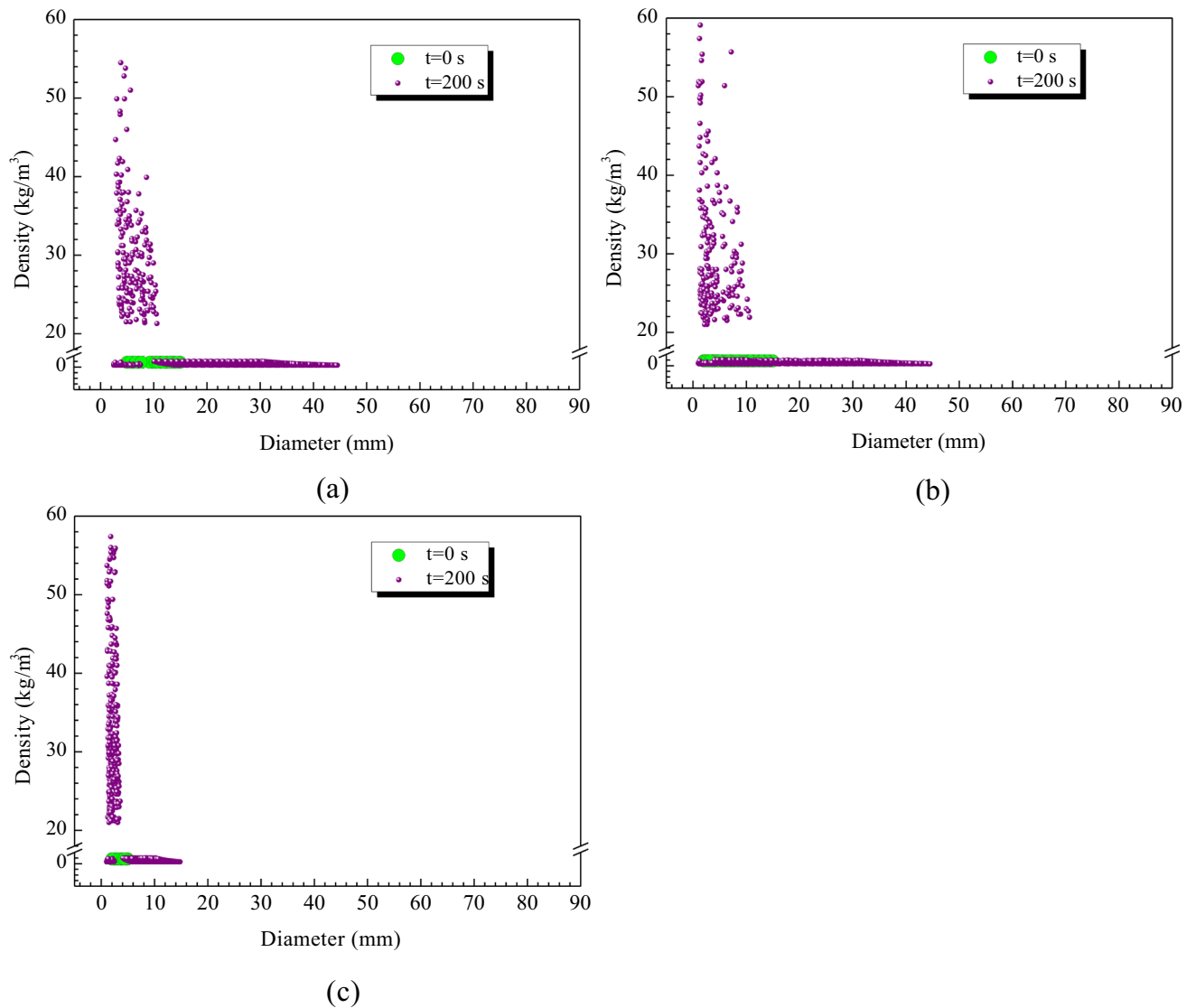
Fig. 19—Density variation of bubbles: (*a*) S-S mode, (*b*) S–P mode, (*c*) P–P mode.

tuyere side is much larger than the porous side, pushing more steel move towards the porous tuyere side, just as revealed by the streamlines on the slag–metal interface. Similar phenomenon is also found in water model experiment, which shows the morphology of flow field through dye tracer injections, just as shown in Figure 18.

E. *Diameter and Density Distribution of Bubbles*

Bubble density and diameter are two important factors that affect bubble floatation.[37,38] The relationship between bubble density and diameter is illustrated by Figure 19. In the S–S mode (Figure 19(a)), bubbles' initial diameter is 0.882 kg/m^3. When the flow field becomes steady, the density distribution rises aggressively because some inclusions are attached by the bubbles. Most of the inclusions are attached by the bubbles with diameter less than 10 mm. Bubble density is ranged from 20 to 60 kg/m^3. By comparison, for the

S–P mode, just as shown in Figure 19(b), more bubbles with bigger density are revealed, indicating that more inclusions are attached by bubbles. The optimal bubble size to attach inclusions is below 0.015 m, and the density is ranged from 20 to 60 kg/m^3. In the P–P mode (Figure 19(c)), bubbles are rather small, the diameters which are entrapped with inclusions are ranged between 1.5 and 10 mm.

The characteristics of plume zone are important for the mixing behavior in a ladle.[39] Figure 20 reveals the averaged velocity on the axes of plume zones. It can be seen from Figure 20(a) that in the S–S mode, the velocity on both plumes are large because the bubbles injected from slot tuyere are bigger than the bubbles that are injected from porous tuyere. That's why the velocity in the S–P mode is obviously asymmetry, just as shown in Figure 20(b) and water model experiments in Figure 18. However, in the P–P mode (Figure 20(c)), the velocity on both sides are quite uniform, not too much different
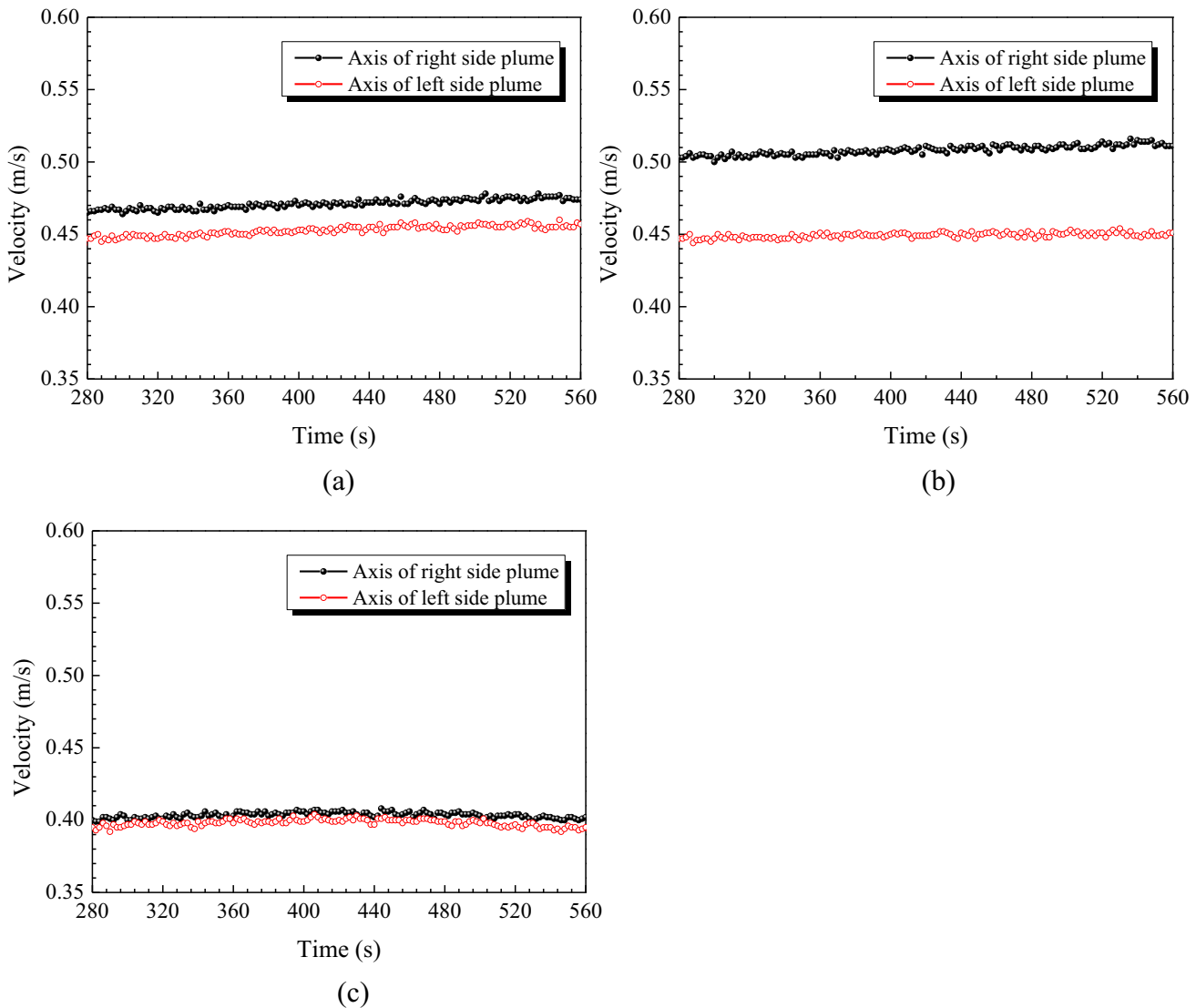
Fig. 20—Comparison of velocity magnitude of bubble plume zone along vertical direction: (*a*) S–S mode; (*b*) S–P mode; (*c*) P–P mode.

after all, because the bubble diameters are rather small and uniform. It can also be seen that the averaged velocity near the right side plume is larger than that near the left side. The reason is because the right side tuyere is further to the wall of ladle, so the friction between wall and fluid is lower than that of left side. That's why the averaged velocity on the left side is lower than that in the right side.

Apart from the results above, the mixing behavior is also obtained, just as shown in Figure 21. The initial position of melt alloy and the monitor points are displayed in Figure 21(a). The mixing time is defined as the time when final mass fraction's differences is within ± 5 pct. Figure 21 shows that the injection mode has

influence the mixing behavior greatly in ladle: The mixing time for the S–S, S–P, P–P mode are 120.45, 109.95, and 135.3 seconds, respectively. This indicates that S–P mode's employment may shorten the mixing time considerably in a real ladle. The reason for this phenomenon is because the recirculation flow near the ladle's bottom is intensified, just as shown in Figure 11.

Figure 22 illustrates the transient distribution of dye tracers. Comparisons are made between different tuyere matches. Easily seen, the mixing speed is more uniform through S–P mode than S–S mode. And also the dead zone is significantly reduced especially near the corner of the ladle bottom because the core of vortex is declined. For the P–P mode, as the stirring energy is low, the
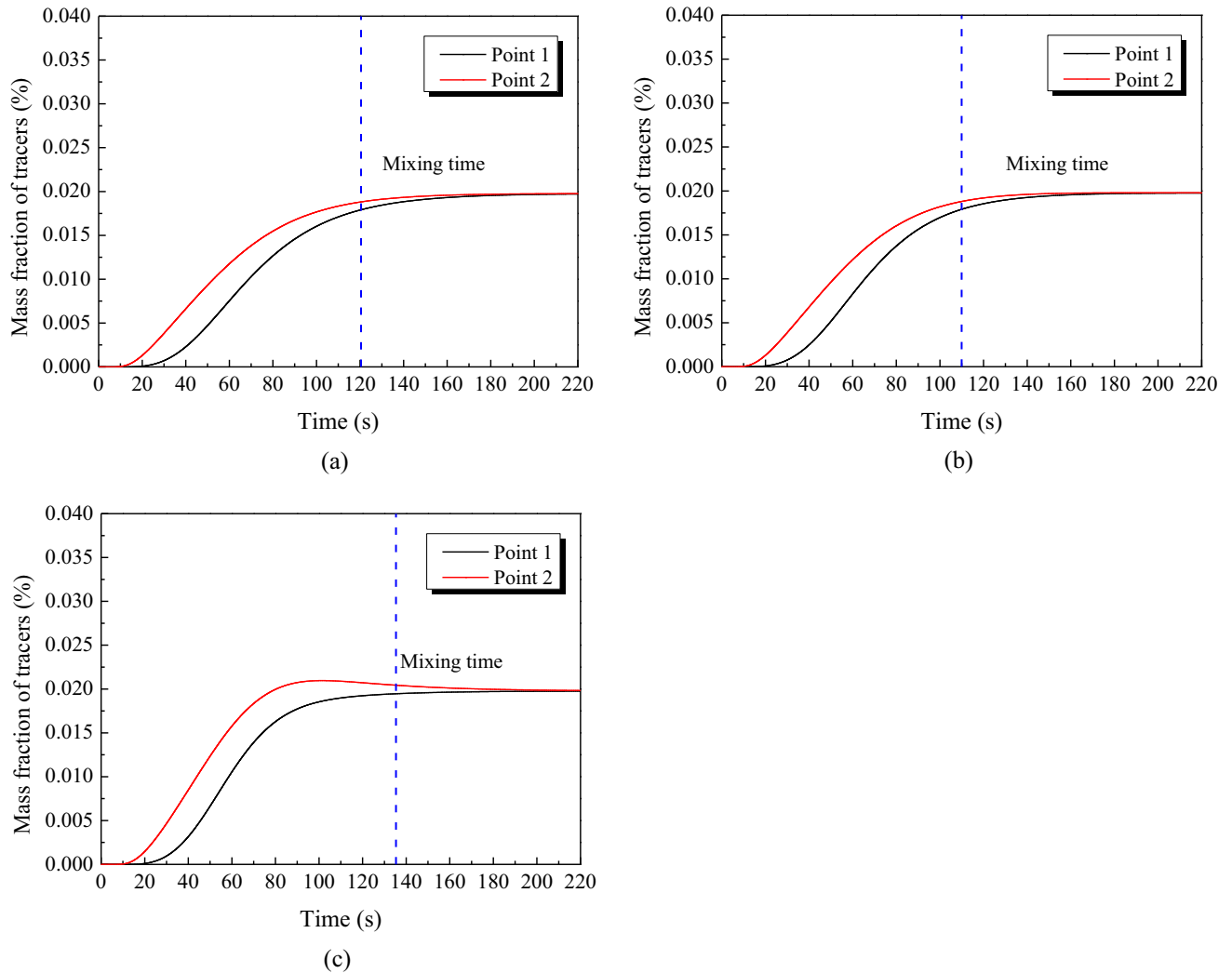
Fig. 21—Time series of mass fractions of dye tracer at different modes: (*a*) S–S mode, (*b*) S–P mode, (*c*) P–P mode.

diffusion rate of dye tracers is quite slow. These results can also be found in Figure 17. All in all, the optimal tuyere match is the S–P mode.

Figure 23 shows the transient percentage of inclusion removements in a ladle. The total monitoring time is 560 seconds. It can be seen from Figure 23 that the percentage of inclusion removement through S–S mode is 29.48 pct, while for the S–P mode the percentage of inclusion removements is 36.34 pct. When it comes to P–P mode, the ratio of inclusion removement firstly increases fast, then the growing speed decreases after 191.15 seconds, however, the percentage of inclusion removement through S–P mode is still higher than that through the S–S mode, reaching 34.1 pct. The same trend is also found in water model experiment (Figure 7). Through comparing with the three tuyere modes, we can come to the conclusion that the S–P mode is optimal for

removing inclusions in steel. The reason is because the S–P mode increases the turbulence and prevents the inclusions recycling downwards with the steel.

IV. CONCLUSION

The main innovation of this work is to propose a new injection mode through a new mathematical model, which is validated through water model result. This modeled is used to describe the aggregation and breakup of two different discrete phases, considering density variation as well as bubble expansion. The following conclusions can be drawn:

1. The ignorance of bubble expansion will lead to the underestimation for the velocity in a ladle, inclusion
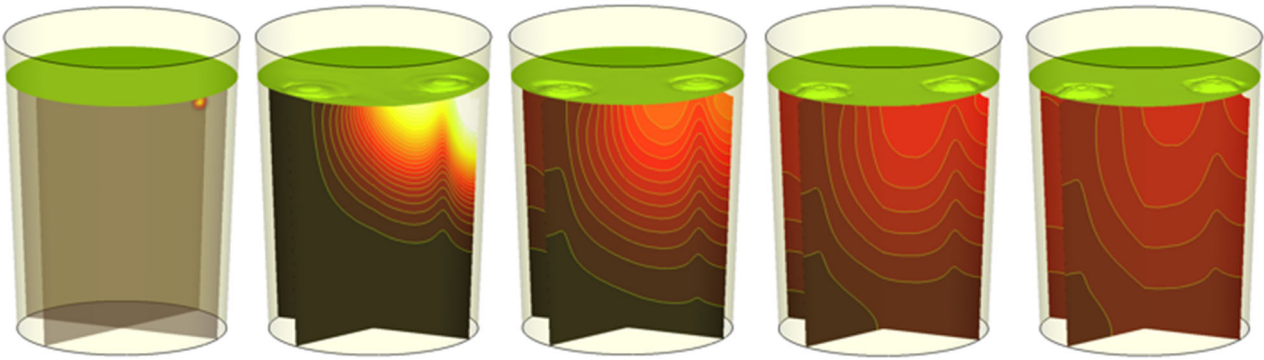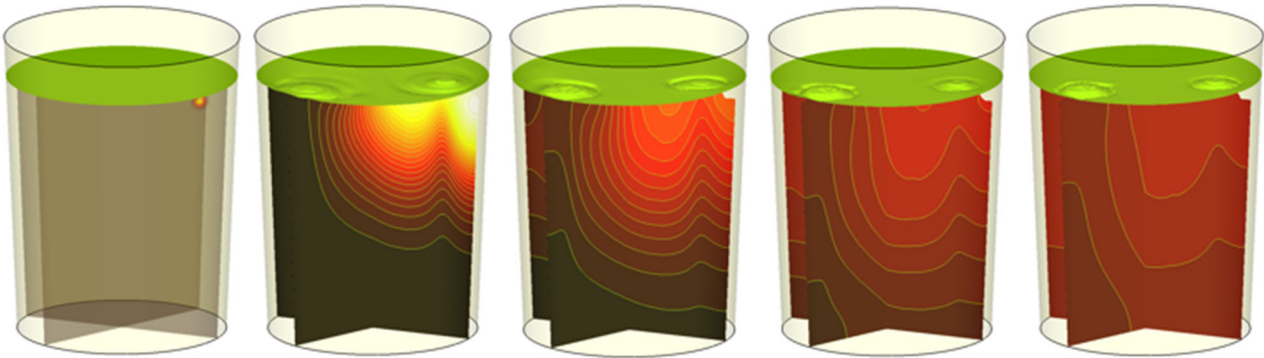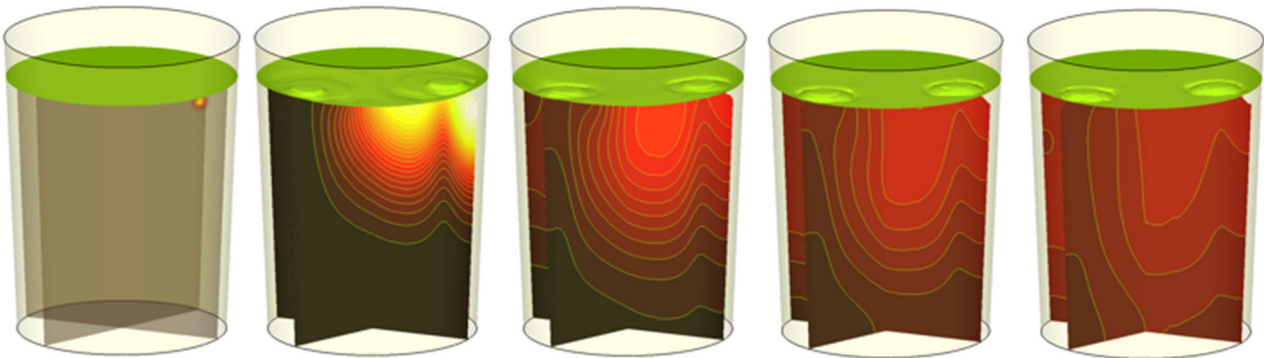
Fig. 22—Comparison of mass fraction of dye tracers at different injection modes: (*a*) 0 s, (*b*) 16 s, (*c*) 36 s, (*d*) 56 s, (*e*) 76 s.

removement as well as efficiency of alloy mixing behavior. Therefore, the bubble expansion effect is suggested to be taken into account in numerical simulation.

2. Due to the bubble expansion, the density of bubbles are mostly decreases to 0.3 to 0.8 kg/m^3. However, when the bubble attach some inclusions, the density significantly increases to about 20 to 60 kg/m^3, and

the optimal bubble diameters that entrap inclusions are ranged from 1.5 to 10 mm.

3. The slot–porous matched dual tuyeres can significantly increasing inclusion removal ratio and shorten the mixing time at the same time. Therefore, this type of injection argon is recommended to use in the future refining.
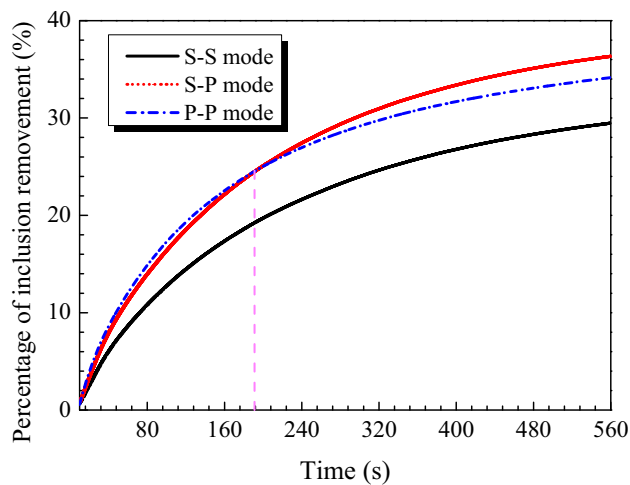
Fig. 23—Percentage of inclusion removement at different modes.

CONFLICT OF INTEREST

The authors declare that they have no conflict of interest.

REFERENCES

1. H.Y. Tang, J.W. Liu, S. Zhang, X.C. Guo, and J.Q. Zhang: *Ironmak. Steelmak.*, 2019, vol. 46(5), pp. 405–15.
2. H.Y. Tang, X.C. Guo, G.H. Wu, and Y. Wang: *ISIJ Int.*, 2016, vol. 56(12), pp. 2161–70.
3. J. Yang, X.H. Wang, M. Jiang, and W.J. Wang: *J. Iron. Steel Res. Int.*, 2011, vol. 18(7), pp. 8–14.
4. F.G. Tan, S.L. Jin, Z. He, and Y.W. Li: *J. Iron Steel Res. Int.*, 2021, vol. 29(4), pp. 628–35.
5. L.F. Zhang and B.G. Thomas: *J. Univ. Sci. Techno. Beijing Miner. Metall. Mater.*, 2006, vol. 13(4), pp. 293–300.
6. S.G. Zheng and M.Y. Zhu: *Acta Metall. Sin.*, 2006, vol. 42(11), pp. 1143–48.
7. B. Trummer, W. Fellner, A. Viertauer, L. Kneis, and G. Hackl: *RHI Bull.*, 2016, vol. 1, pp. 35–38.
8. L. Wang, H.G. Lee, and P. Hayes: *ISIJ Int.*, 1996, vol. 36(1), pp. 7–16.
9. Y.B. Yin, J.M. Zhang, H.T. Ma and Q.H. Zhou: *Steel Res. Int.*, 2021, vol. 92(5), pp. 1–11.
10. Y.B. Yin and J.M. Zhang: *ISIJ Int.*, 2021, vol. 61(3), pp. 853–64.
11. Y.D. Wu, Z.Q. Liu, F. Wang, B.K. Li, and Y. Gan: *Powder Technol.*, 2021, vol. 387, pp. 325–35.
12. Z.Q. Liu, F.S. Qi, B.K. Li, and S.C.P. Cheung: *Int. J. Multiph. Flow*, 2016, vol. 79, pp. 190–201.
13. Y. Zhou, Y.C. Dong, H.C. Wang, S.J. Wang, and Y.B. Liu: *J. Iron Steel Res. Int.*, 2003, vol. 10(4), pp. 8–12.
14. J.S. Zhang, S.F. Yang, J.S. Li, H.Y. Tang, and Z.Y. Jiang: *High Temp. Mater. Processes*, 2018, vol. 37(1), pp. 25–32.
15. Y.B. Yin and J.M. Zhang: *J. Iron Steel Res. Int.*, 2022, vol. 29(2), pp. 247–62.
16. R. Krishna and J.M.V. Baten: *Chem. Eng. Res. Des.*, 2001, vol. 79(3), pp. 283–309.
17. D.Q. Geng, H. Lei, and J.C. He: *ISIJ Int.*, 2010, vol. 50(11), pp. 1597–1605.
18. T. Hibiki and M. Ishii: *Int. J. Heat Mass Transf.*, 2002, vol. 45(11), pp. 2351–72.
19. A. Kitagawa, K. Sugiyama, and Y. Murai: *Int. J. Multiph. Flow*, 2004, vol. 30(10), pp. 1213–34.
20. Z. Xiao and R.B. Tan: *AIChE J.*, 2006, vol. 52(1), pp. 86–98.
21. J. Sanyal, D.L. Marchisio, O. Fox, and K. Dhanasekharan: *Ind. Eng. Chem. Res.*, 2005, vol. 44(14), pp. 5063–72.
22. H.A. Jakobsen, H. Lindborg, and C.A. Dorao: *Ind. Eng. Chem. Res.*, 2005, vol. 44(14), pp. 5107–51.
23. Z. Sha, A. Laari, and I. Turunen: *Chem. Eng. Technol.*, 2006, vol. 29(5), pp. 550–59.
24. D. Colella, D. Vinci, R. Bagatin, M. Masi, and E.A. Bakr: *Chem. Eng. Sci.*, 1999, vol. 54(21), pp. 4767–77.
25. E. Olmos, C. Gentric, C. Vial, G. Wild, and N. Midoux: *Chem. Eng. Sci.*, 2001, vol. 56(21), pp. 6359–65.
26. W.J. Liu, J. Lee, X.P. Guo, A.K. Silaen, and C.Q. Zhou: *ISIJ Int.*, 2018, vol. 90(4), pp. 1–10.
27. X.L. Li, B.K. Li, Z.Q. Liu, D.Y. Wang, T.P. Qu, S.Y. Hu, C.J. Wang, and R.Z. Gao: *Metall. Mater. Trans. B.*, 2021, vol. 52B, pp. 3246–64.
28. X.L. Li, B.K. Li, Z.Q. Liu, R. Niu, Q. Liu and X.C. Huang: *Steel Res. Int.*, 2019, vol. 90(3), pp. 1–13.
29. Z.Q. Liu, B.K. Li, L.J. Xiao, and Y. Gan: *Acta Metall. Sin.*, 2022, vol. 58(10), pp. 1236–52.
30. Z.Q. Liu, Y.D. Wu, and B.K. Li: *Powder Technol.*, 2020, vol. 374, pp. 470–81.
31. L.M. Li, Z.Q. Liu, and B.K. Li: *J. Iron Steel Res. Int.*, 2015, vol. 22(1), pp. 30–35.
32. Q. Li, J.C. Cheng, C. Yang, and Z.S. Mao: *Chem. Eng. Technol.*, 2017, vol. 40(10), pp. 1792–1801.
33. S.F. Chen, H. Lei, H.C. Hou, C.Y. Ding, H. Zhang, and Y. Zhao: *J. Market. Res.*, 2021, vol. 15, pp. 5141–50.
34. G.J. Chen and S.P. He: *J. Market. Res.*, 2020, vol. 9(3), pp. 3318–29.
35. Q. Cao and L. Nastac: *JOM*, 2018, vol. 70(10), pp. 2071–81.
36. Q. Wang, C. Liu, L.P. Pan, Z. He, and G.Q. Li: *Metall. Mater. Trans. B*, 2022, vol. 53B, pp. 1617–30.
37. W.D. Yang, Z.G. Luo, N.N. Zhao and Z.S. Zou: *Metals*, 2020, vol. 10(9), pp. 1–15.
38. M. Tanno, J. Liu, X. Gao, S.J. Kim, S. Ueda, and S. Kitamura: *Metall. Mater. Trans. B*, 2017, vol. 48B, pp. 2913–21.
39. Y. Liu, M. Ersson, H.P. Liu, P.G. Jönsson, and Y. Gan: *Metall. Mater. Trans. B*, 2019, vol. 50B, pp. 555–77.